The International Journal of Advanced Manufacturing Technology (2022) 120:1265–1280
https://doi.org/10.1007/s00170-022-08844-7

ORIGINAL ARTICLE

Effect of NbC in-situ synthesis on the microstructure and properties of pre-placed WCoB-TiC coating by laser cladding

Hao Zhang[1] · Yingjun Pan[1] · Yang Zhang[2] · Guofu Lian[3] · Qiang Cao[3] · Xingyu Zhu[1]

Received: 8 December 2021 / Accepted: 27 January 2022 / Published online: 11 February 2022

Abstract

WCoB-TiC composite coatings with in-situ formation of NbC were fabricated on the surface of an AISI 1045 substrate by laser cladding. The geometric characteristics, microstructure, microhardness, and fracture toughness of coatings were investigated by means of an optical microscope (OM), a scanning electron microscope (SEM), energy-dispersive spectroscopy (EDS), X-ray diffraction (XRD), an electron probe microanalyzer (EPMA), and a microhardness tester. In addition, the elastic constants and bulk property of the reinforced phases were investigated by first principles calculation. The results showed that a reliable metallurgical bonding was formed between the coating and the substrate and in-situ synthesized reinforcement phases of the coating consisted of WCoB, W_2CoB_2, TiC, NbC, (Nb,Ti,W)C, and traces of Nb_2C. The dilution rate and porosity had a negative effect with the addition of Nb. According to the results of SEM, EDS, and EPMA, Nb was diffused uniformly in the TiC structure. The NbC phase had the highest hardness among all in-situ synthesized reinforcement phases, which reached 24.525 GPa, while Nb_2C reflected the strongest metallicity. The microhardness and fracture toughness of the coating were increased firstly and then decreased following the increase of Nb content, and when the Nb addition was 4 wt%, the coating had the highest average microhardness and fracture toughness (1755.42 $HV_{0.5}$, 8.23 $MPa{\cdot}m^{1/2}$, respectively). The microhardness and fracture toughness was 24% and 30% higher than that of the coating without Nb addition, respectively. From the crack propagation morphology of coatings, all coatings had fine transgranular fracture.

Keywords Laser cladding · NbC · WCoB-TiC composite coating · Fracture toughness · Microhardness

1 Introduction

In recent years, boride-based cermets, especially ternary boride–based cermets, have attracted considerable attention due to their excellent high-temperature oxidation resistance, high hardness, perfect chemical stability, and high strength [1–4]. Hence, ternary boride–based cermets have been widely applied to the iron and steel industry, automotive mold industry, and aerospace [2, 5]. In these ternary boride–based cermets, typical Mo_2NiB_2 [6–8], Mo_2FeB_2 [9–11], and WCoB [12, 13] were studied. Among these three ternary boride–based cermets, WCoB is a complex ternary boride with extremely high hardness, excellent oxidation resistance, and high thermodynamic stability [14–17]. However, due to its brittleness, poor sinterability, and responsive reactivity with metals, the extension of its industrial applications is limited [18–20].

Zhang et al. [14] found that the hardness of WCoB and W_2CoB_2 were decreased with the increased amount of Mn doping by five hardness models. Zhang et al. [21] fabricated Cr-doped WCoB-based cermets with spark plasma sintering and studied the microstructure and mechanical properties through first principles calculation. They found that the maximum value of Vickers hardness was 1751 $HV_{0.5}$ at 9.356 wt% Cr doping content. Wang et al. [22] prepared WC-WCoB coating and achieved simultaneous improvement in the hardness and fracture toughness of WC-WCoB coating.

✉ Yingjun Pan
hbwhpyj@163.com

✉ Yang Zhang
yzhang@wcu.edu

[1] The State Key Laboratory of Refractories and Metallurgy, Wuhan University of Science and Technology, Wuhan 430081, People's Republic of China

[2] School of Engineering + Technology, Western Carolina University, Cullowhee, NC 28723, USA

[3] School of Mechanical & Automotive Engineering, Fujian University of Technology, Fuzhou 350118, People's Republic of China

However, there are few reports about WCoB-TiC coating by laser cladding. With the continued development, laser cladding has become an important technique for surface modification, which utilizes a high-energy laser beam to heat the alloy powder and substrate simultaneously to form a new cladding layer [23–25]. Compared with the conventional surface-strengthening technology, laser cladding has advantages of low dilution rate, reduced thermal impact, and excellent metallurgical bonding between the coating and substrate [26, 27]. Besides, the prepared coating has advantages of high hardness and wear resistance. Thus, it can be used to improve the wear resistance, corrosion resistance, heat resistance, and oxidation resistance of the substrate surface [23, 28, 29]. Owing to the advantages of laser cladding, it has been widely used in the fields of aerospace, marine, petroleum, and high-value part remanufacturing [25–27].

To overcome the mechanical property limitations of value parts, in recent years, in-situ synthesized reinforcement particles by laser cladding have attracted more attention from scholars. Yan et al. [30] concluded that AlCoCrFeNiSi-based high-entropy alloy coating can significantly improve the wear resistance of an H13 substrate with in-situ forming Ti(C,N) by laser cladding. Hu et al. [31] found that the wear resistance of Ni-Ta coating and Ni-Ta-C coating was 2 times and 4 times higher than that of a 5Cr5MoSiV1 steel substrate by in-situ synthesized Ni_3Ta-TaC. Liu et al. [32] discussed the effect of in-situ TiC-reinforced AlCoCrFeNi-based high-entropy alloy composite coatings prepared utilizing laser cladding. They concluded that the $AlCoCrFeNiTi_{1.0}$ HEA composite coating had the highest volume fraction of TiC particles phase (2.6%) and the best wear resistance. However, according to the literature [33, 34], among all carbide phases, NbC possesses outstanding mechanical and physical properties, such as high hardness, high melting point (which is good for high-temperature applications), and low density (which can reduce the cost). Thus, NbC has become more attractive because of these advantages.

In this study, the geometric characteristics, microstructure, microhardness, fracture toughness, and microstructure evolution of in-situ synthesized NbC/WCoB-TiC coatings prepared by laser cladding were investigated. The distribution and existing form of Nb were analyzed. Combined with the first principles, the elastic constants and metallicity of all in-situ synthesized reinforcement phases were also analyzed. The results of this work will be beneficial for the preparation of WCoB-TiC coating by laser cladding and selection of suitable Nb addition to the coating to improve the mechanical properties.

2 Experimental procedures and calculation details

2.1 Materials

The AISI 1045 steel was selected as the substrate (40 mm × 20 mm × 10 mm). The laser beam diameter was set as 4 mm. Raw cladding raw powder was prepared from a mixture of WC (2–3 μm, purity 99.8%), TiB_2 (2–3 μm, purity 99%), and Co powder (2–3 μm, purity 99.9%). The elemental composition of the AISI 1045 steel substrate and Nb powder (3–5 μm, purity 99.9%) is shown in Tables 1 and 2, respectively.

2.2 Experimental procedures

The surface of AISI 1045 steel substrate was cleaned by ethanol before conducting laser cladding. The raw powder (WC, TiB_2, Co) was mixed in an MITR-YXQM-2L ball mill machine (MITR, Changsha, China). During the ball milling process, the main plate rotation was 150 rpm, the planetary disk rotation was 75 rpm, the ball to powder weight ratio was 4:1, and the ball milling time was 48 h. Then, 5 wt% polyvinyl alcohol (PVA) binder was added into the mixed raw powder. Afterward, the mixing was continued with adding various Nb (wt%) under the same ball milling parameters. After the completion of mixing, the powder was pre-placed as 1-mm thickness on the surface of the AISI 1045 substrate under the pressure of 100 MPa for 60 s, and then placed in a vacuum dryer for an additional 2 h at a temperature of 120 °C. The mass ratio of WC, TiB_2, and Co in the raw cladding powder remained unchanged (WC: 59 wt%; TiB_2: 21 wt%; Co: 20 wt%). The experimental design is shown in Table 3.

Table 1 Elemental composition (wt%) of the AISI 1045 steel substrate

Element	C	Si	Mn	Cr	Ni	Cu	Fe
Component	0.42–0.50	0.17–0.37	0.50–0.80	≤ 0.25	≤ 0.30	≤ 0.25	Rest

Table 2 Elemental composition (wt%) of the Nb powder

Element	Ni	Si	Mn	O	Cr	N	Fe	Nb
Component	0.002	0.002	0.022	0.035	0.001	0.023	0.001	Rest

The laser cladding was carried out by using the laser cladding system (Fig. 1), which includes a laser system (YLS-3000, IPG, Burbach, Germany), a laser cladding nozzle with a 300-mm focal length (FDH0273, Laser Mech, Novi, MI, USA), an industrial robot (M-710iC/50, FANUC, Yamanashi, Japan), a water-cooling system (TFLW-4000WDR-01–3385, Sanhe Tongfei, Sanhe, China), a control system (PLC, Mitsubishi, Japan), and a laser pulse control system (SX14-012PULSE, IPG, Burbach, Germany). Argon gas was used as protective gas to protect the molten pool of the coating. In order to enable the in-situ synthesis to proceed successfully, the parameters of this research were set at laser power of 2500 W, scanning speed of 7 mm/s, and shielding gas flow of 10 NL/min.

2.3 Characterization

Sample preparation for characterization includes cutting to size 10 mm × 5 mm × 5 mm, setting, grinding, and polishing. Then, the prepared sample was immersed in a solution with 1:1:10 ratio of $K_3[Fe(CN)_6]_4$:NaOH:H_2O for 20 s, and then cleaned with alcohol ultrasonically.

The ZEISS Axio Plan2 optical microscope (OM) (Zeiss, Shanghai, China) was used to analyze the cross-sectional morphology of the coating. The Image-Pro Plus 6.0 software was used to measure the cross-sectional height (H), width (W), and area (A_1) of the cladding layer. Besides, the height (h) and area of melting zone (A_2) and the height of the heat-affected zone were also measured. The detailed schematic is shown in Fig. 2; the dilution rate (D) and porosity were calculated according to formulas (1) and (2), where A_p is the sum of all the pore area, which was also measured by the Image-Pro Plus 6.0 software.

Table 3 Composition of different specimens

Specimen number	Raw powder/wt%	Nb/wt%
C1	100	0
C2	98	2
C3	96	4
C4	94	6

$$D = \frac{A_2}{A_1 + A_2} \times 100\% \tag{1}$$

$$\text{porosity} = \frac{A_p}{A_1 + A_2} \times 100\% \tag{2}$$

The X-ray diffraction (XRD) analysis was conducted with X-Pert Pro MPD systems (PANalytical, the Netherlands) equipped with Cu Kα radiation ($\lambda = 0.15418$ nm) at 400 kV and 200 mA. The 2θ range was 10–90°, and the scan step was 0.05°; the measured time was 10 s per step. The microstructure of the coating was observed by a field emission scanning electron microscope (Nova 400 Nano SEM, FEI, USA) and field emission electron probe microanalyzer (FE-EPMA, EPMA-8050G, Shimadzu, Japan). Also, element analysis was performed using energy-dispersive X-ray spectroscopy (EDS) (INCA IE 350 PentaFET X-3, Oxford, UK).

An HX-500 microhardness tester (Laizhou Yutong Test Instrument Co. LTD, Laizhou, Shandong, China) was utilized to measure the microhardness of the cross section of the coating with a 500-g force applied for a 10-s duration. The fracture toughness (K_{IC}) was conducted on the cross section of each specimen with a load of 10 kg applied for a 10-s duration according to Eqs. (3) and (4) [35–37], and Fig. 3 shows the schematic diagram of Vickers indentation measurement of K_{IC}. In order to guarantee the accuracy of experiments, the value of the microhardness and K_{IC} of each specimen was obtained by averaging three repetitive measurements. The fracture energy (Γ) can be calculated by Eq. (5) [35, 37].

$$K_{IC} = 0.16\text{HV}a^2c^{-3/2} \tag{3}$$

$$\text{HV} = 0.464P/d^2 \tag{4}$$

$$\Gamma = 2\xi^2 p^2/c^3 \tag{5}$$

where a is the half-length of the indentation diagonal, c is the half-crack length measured from the middle of the indentation to the tip of crack, P is the loading force (98 N), and ξ is the geometry factor of the Vickers penetrator ($\xi = 0.016$) [37].

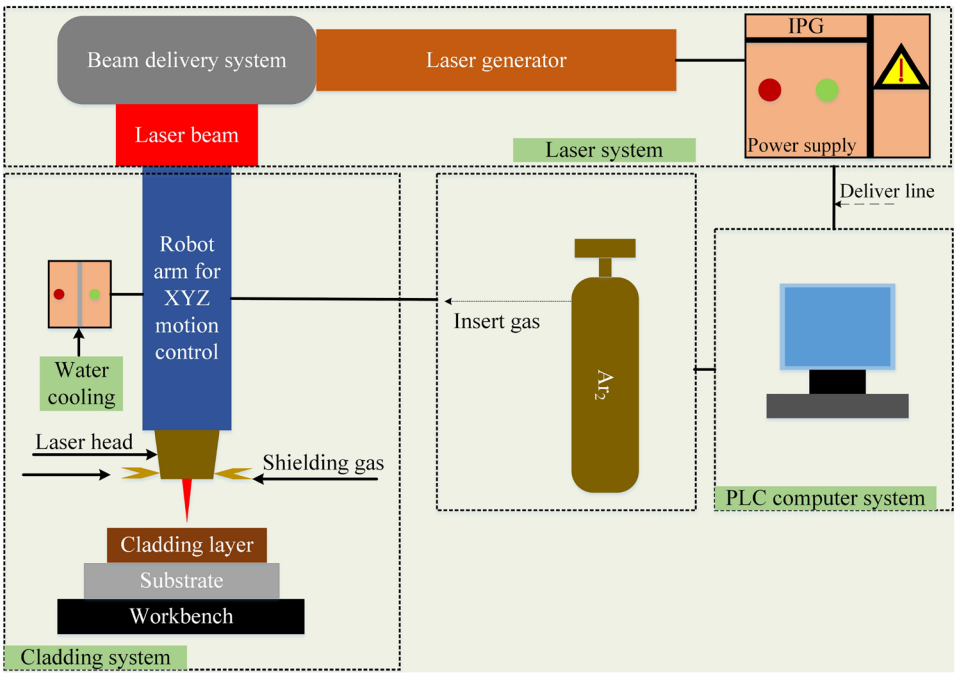

Fig. 1 Laser cladding system schematic illustration

2.4 Calculation details

The BIOVIA Materials Studio 2019 (19.1.0) software was used to accomplish first principles calculation based on the Cambridge Sequential Total Energy Package (CASTEP) code of density functional theory (DFT) in the research [38, 39]. During the calculation, the generalized gradient approximation (GGA) with the Perdew-Burke-Ernzerhof (PBE) functional was employed as the exchange–correlation energy functions [40, 41]. NbC and TiC have a cubic structure, the lattice parameter of NbC is $a = 4.470$ Å, and the lattice parameter of TiC is $a = 4.328$ Å. W_2CoB_2, WCoB, and Nb_2C have an orthorhombic structure; the lattice parameter of W_2CoB_2 is $a = 7.075$ Å, $b = 4.564$ Å, and $c = 3.177$ Å; the lattice parameter of WCoB is $a = 5.745$ Å, $b = 3.203$ Å, and $c = 6.652$ Å; and the lattice parameter of WCoB is $a = 10.920$ Å, $b = 4.974$ Å, and $c = 3.090$ Å.

3 Results

3.1 Cross-sectional morphology of coating

Figure 4 shows the cross-sectional morphologies of coatings with different Nb additions. It is observed that the all the coatings consisted of the cladding zone (CZ), bonding

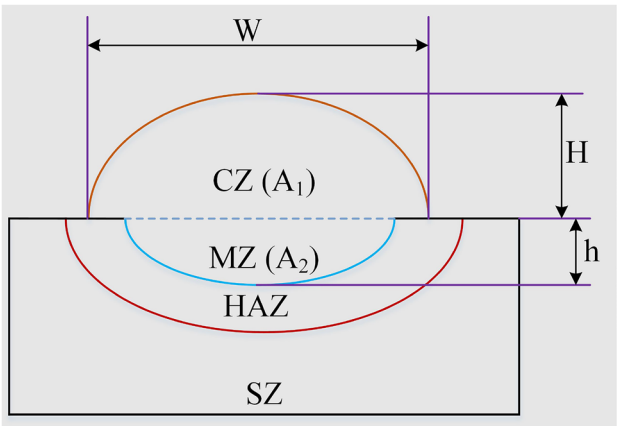

Fig. 2 Schematic illustration of cross section of the cladding layer

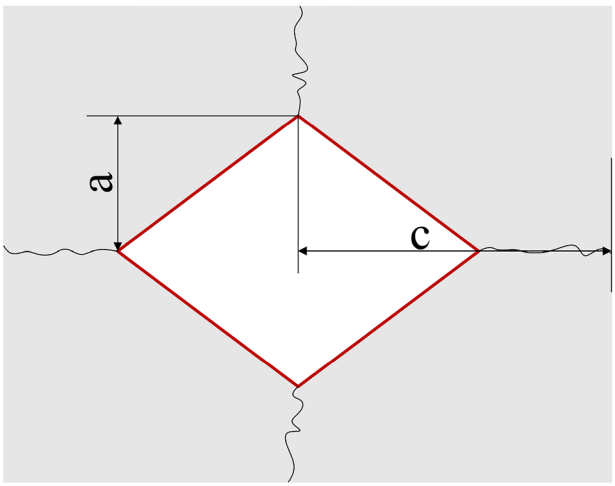

Fig. 3 Schematic diagram of Vickers indentation measurement of K_{IC}

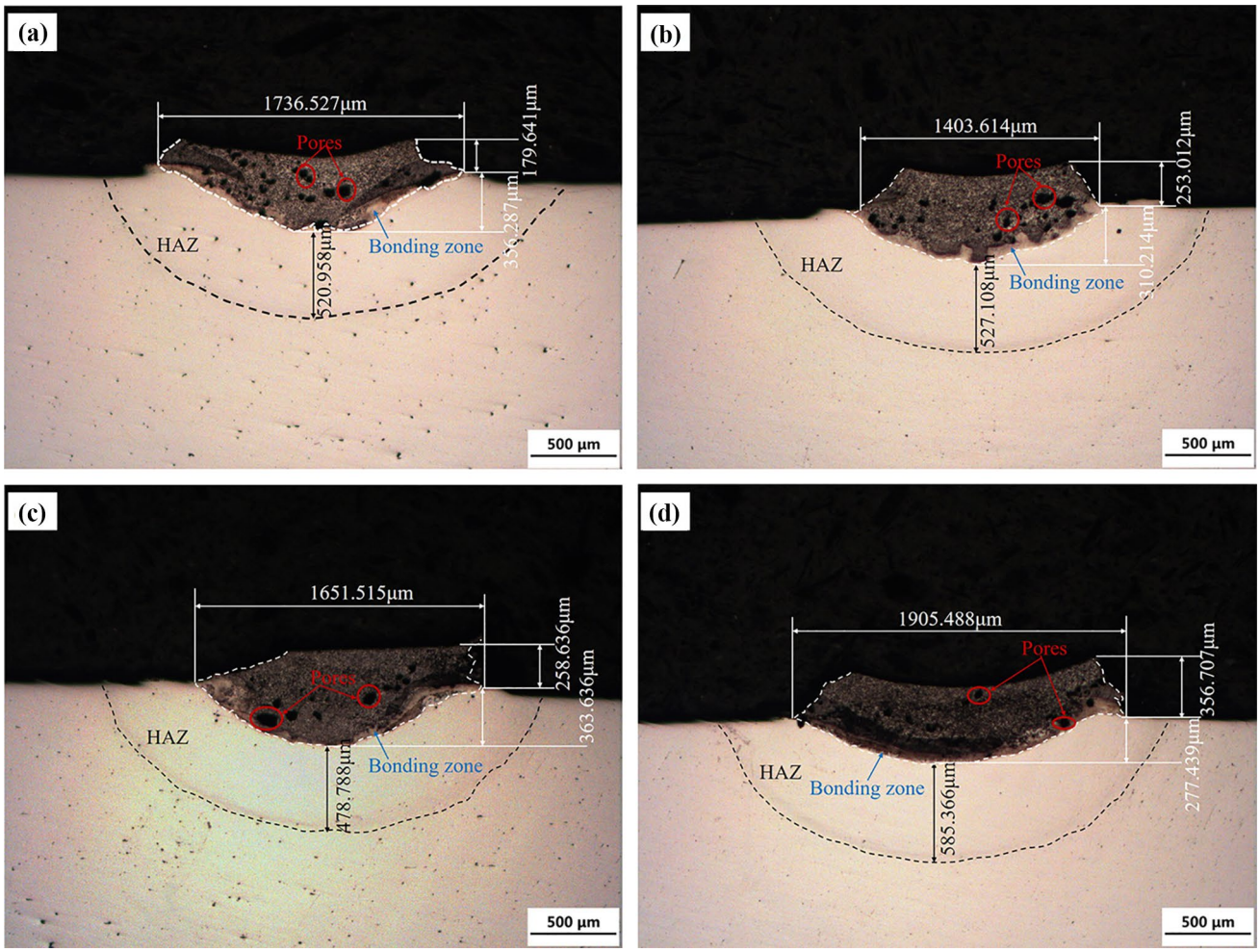

Fig. 4 Cross-sectional morphologies of coatings: **a** C1, **b** C2, **c** C3, and **d** C4

zone (BZ), heat-affected zone (HAZ), and substrate (SZ). The outer line of coating was marked with a white dotted line, while the HAZ was marked with a black dotted line. Noticeable pores were observed in the coating, which were more distributed uniformly in the coating, whereas an excellent bonding zone was formed between the coating and the substrate. The depth of the HAZ in different settings was indicated by the black double-headed arrows and marked in Fig. 4, which ranged from 478.78 to 585.366 μm.

In order to accurately analyze the geometric characteristic change in the coating with different Nb additions, Fig. 5 is plotted. It can be found that following the increase of the Nb addition, the dilution rate and porosity decreased. During the laser cladding process, the laser induced high energy to melt the pre-placed powder and part of substrate to form the molten pool. With the increase of Nb addition, due to its high melting temperature, more energy was absorbed by the powder, leading to the increased energy absorption in the molten pool. In contrast, more Nb would promote the reaction of C atoms in the coating by high laser energy. Hence, the process can decrease the reaction of C atoms in the coating and O atoms in the near-top region of the coating, which could decrease the trend of generating the CO_2

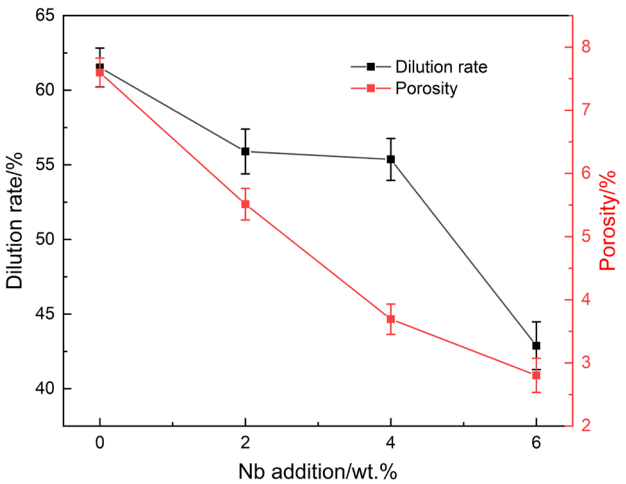

Fig. 5 Dilution rate and porosity of coatings at different Nb additions

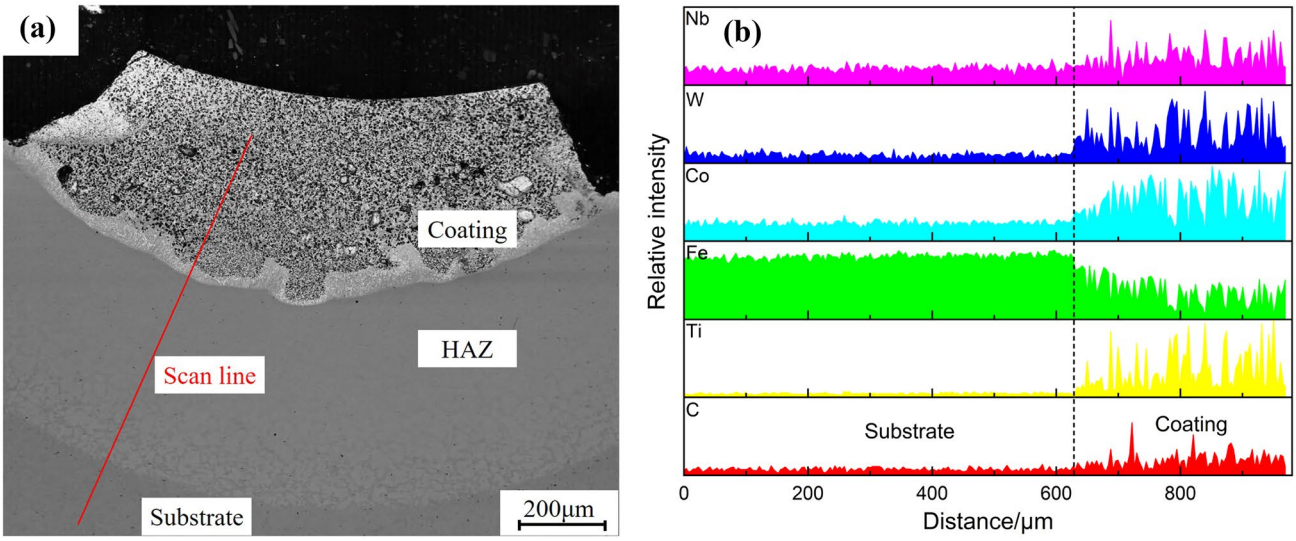

Fig. 6 **a** Cross-sectional morphology of C2 coating; **b** elemental distribution

or CO gas [42], and the porosity will decrease. In the same way, the melting area of the substrate (A_2) decreased as the decreased energy absorption by the substrate, which resulted in the decrease of the dilution rate.

Figure 6a shows the cross-sectional morphology of C2 coating, and the EDS linear scanning of elemental distribution between the coating and the substrate is shown in Fig. 6b. According to the materials of laser cladding and Fig. 6b, the AISI 1045 steel substrate had the highest Fe element content, which decreased gradually from the substrate to the coating, while the Nb, W, Co, and Ti elements showed a contrary trend. Based on the EDS linear scanning analysis, diffusion occurred between the coating and the substrate; it was suggested that an excellent metallurgical bonding was formed.

3.2 Phase constitution and microstructure

Figure 7 shows the X-ray diffraction patterns of WCoB-TiC coatings with different Nb additions, which can clearly demonstrate the effect of Nb addition on the coating. The results showed that all coatings were mainly composed of WCoB, W_2CoB_2, TiC, TiB_2, Co_2B, Fe, and $Fe_{11}Co_5$. When the Nb powder was added to the coating, the diffraction peaks of NbC, Nb_2C, and (Nb,Ti,W)C solid solution were detected in the coatings C2, C3, and C4. Moreover, the C4 coating had the strongest NbC phase peak, which was consistent with the addition of Nb powder. Besides, the coating had a weak Nb_2C phase peak. During the laser cladding process, under the action of strong convection in the molten pool, the Fe element in the substrate diffused into the coating and reacted with the Co element in the coating to form a new phase ($Fe_{11}Co_5$). The diffraction peak of $Fe_{11}Co_5$ decreased with the increase of Nb addition; this was due to the effect of dilution rate. However, due to the high dilution rate of the coating and the rapid heating and cooling characteristics of laser cladding, part of the Fe element cannot react with other elements, so it existed in the coating in the form of Fe, and the peak decreased with the decrease of the dilution rate. Under the effect of high laser energy, TiB_2, WC, and Co went through different levels of melting and decomposition, and developed to form new phases in the coating, including WCoB, W_2CoB_2, and TiC. Due to the similar atomic radius among Ti, Nb, and W, some Ti atoms were replaced by Nb and W in TiC and formed (Nb,Ti,W)C solid solution. NbC and Nb_2C were detected in the coatings of C2, C3, and C4. As a result, they were in-situ synthesized in the coating.

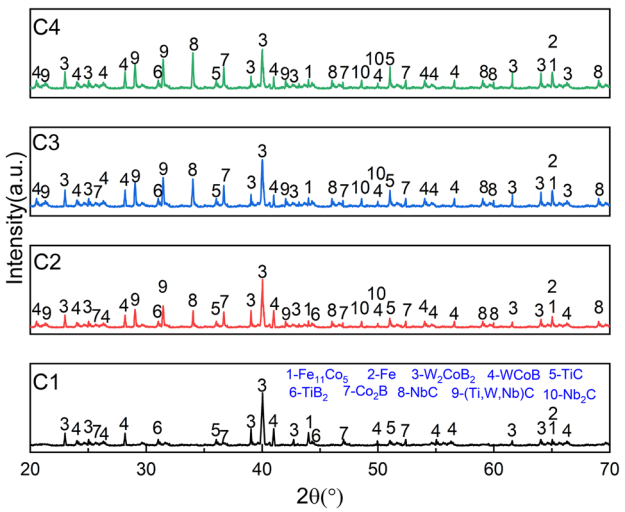

Fig. 7 XRD patterns of coatings with different Nb additions

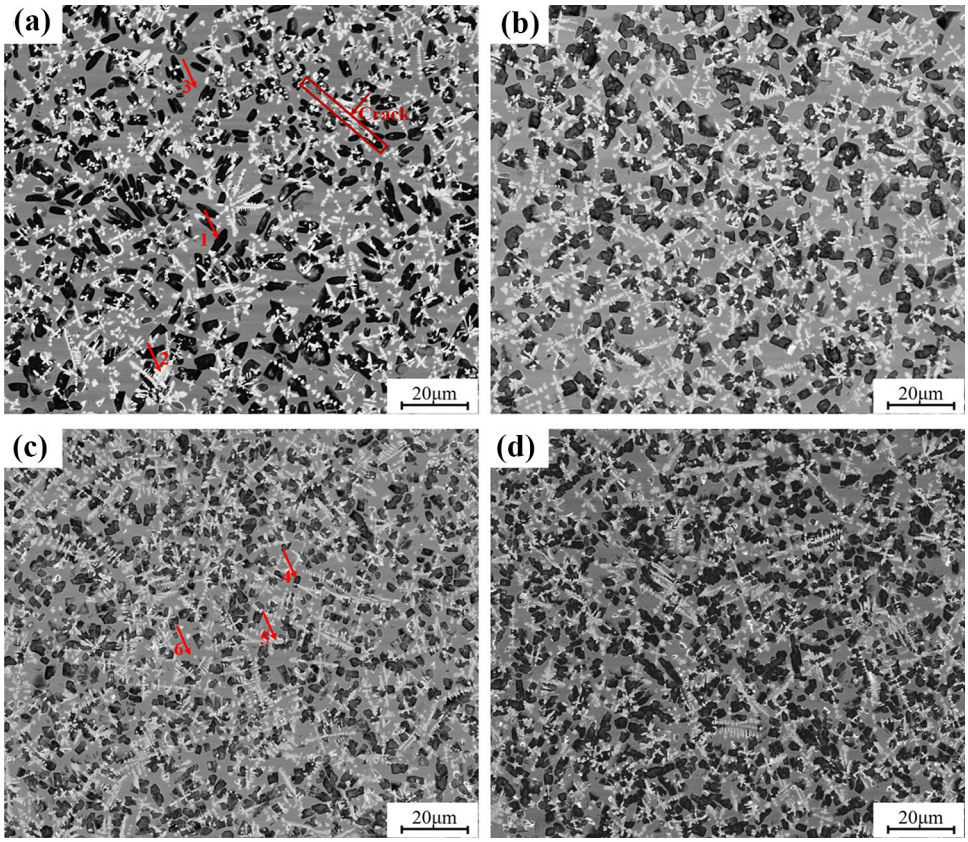

Fig. 8 The middle region backscattered electron (BSE) images of coatings: **a** C1, **b** C2, **c** C3, and **d** C4

The microstructure of the coating could determine its mechanical properties, so it is important to analyze the microstructure of coatings with different Nb additions. Figure 8 exhibits the backscattered electron (BSE) microstructure images of the coatings with different Nb additions. It can be clearly seen that all coatings were composed of a black phase, a white phase, and a gray phase. Besides, an obvious crack can be found in the C1 coating without Nb addition, which was harmful to its mechanical properties. When the coating had no Nb addition, the hard phase of black was nearly rectangle in shape; the white phase was a dendritic crystal structure and had a more obvious secondary dendrite arm. Moreover, the black phase and white phase were distributed uniformly in the gray phase. With the increase of Nb addition, the coating appeared with a fine black phase and the dendritic crystal structure had no obvious secondary dendrite arm. It can be found that with the addition of Nb, the hard phase grain growth was significantly inhibited. The grain size was significantly reduced, which was called fine-grained strengthening [43]. However, it was noticed that with the Nb addition increased to 6 wt%, the coating had obvious fine grain agglomeration phenomenon of hard phase particles, which was not beneficial to improving the mechanical properties of the coating [44].

In order to understand the component of different color phases, the element concentrations and EDS results according to Fig. 8a are shown in Table 4 and Fig. 9a, respectively. These results can confirm that the main elements in the black phase (spectrum 1) were Fe and Co. They suggested that the black phase was composed of $Fe_{11}Co_5$, Fe, and little TiB_2

Table 4 EDS elemental analysis of different positions marked in Fig. 8a, c

Spectrum	Weight%						Atomic%					
	C	Ti	Fe	Co	W	Nb	C	Ti	Fe	Co	W	Nb
1	1.58	3.80	71.13	19.92	3.58	-	7.14	4.30	69.15	18.35	1.06	-
2	6.74	29.44	16.77	7.48	39.57	-	30.86	33.80	16.52	6.98	11.84	-
3	2.54	1.48	69.72	19.66	6.61	-	11.35	1.66	67.12	17.93	1.93	-
4	6.79	9.44	49.77	23.33	8.25	2.41	26.67	9.29	42.03	18.67	2.12	1.23
5	8.64	26.24	12.60	5.68	36.32	10.52	37.86	28.83	11.87	5.08	10.40	5.96
6	1.94	3.31	58.97	28.66	6.22	0.90	8.88	3.80	58.14	26.78	1.86	0.53

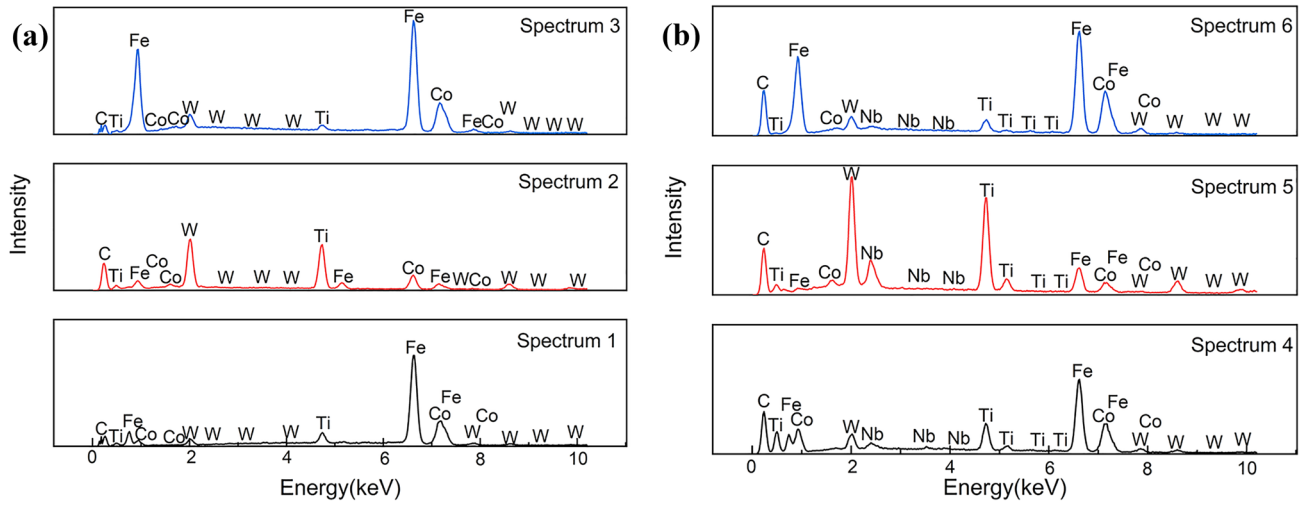

Fig. 9 EDS analysis of different color phases of coatings marked in Fig. 8: (**a**) marked region in Fig. 8a; (**b**) marked region in Fig. 8c

and WCoB. The main elements in the white phase (spectrum 2) were Ti and C, and the atomic ratio Ti/C was about 1:1, and the atomic ratio W/Co was about 2:1 without considering the measurement error of the light element (such as B) content by the SEM, which suggested that the white phase was composed of W_2CoB_2 and TiC. The main elements in the gray phase (spectrum 3) were composed of Fe and Co, which consist of $Fe_{11}Co_5$, Fe, and Co_2B. According to the results of Fig. 9a, the intensity of Fe and Co in spectrum 3 was higher than that in spectrum 1, which suggested the accuracy of the phase. Besides, the results of spectra 4, 5, and 6 in Fig. 8c are shown in Table 4 and Fig. 9b. Compared with Fig. 9a EDS results, the results for the C3 coating had Nb element distribution. The Nb element mostly existed in

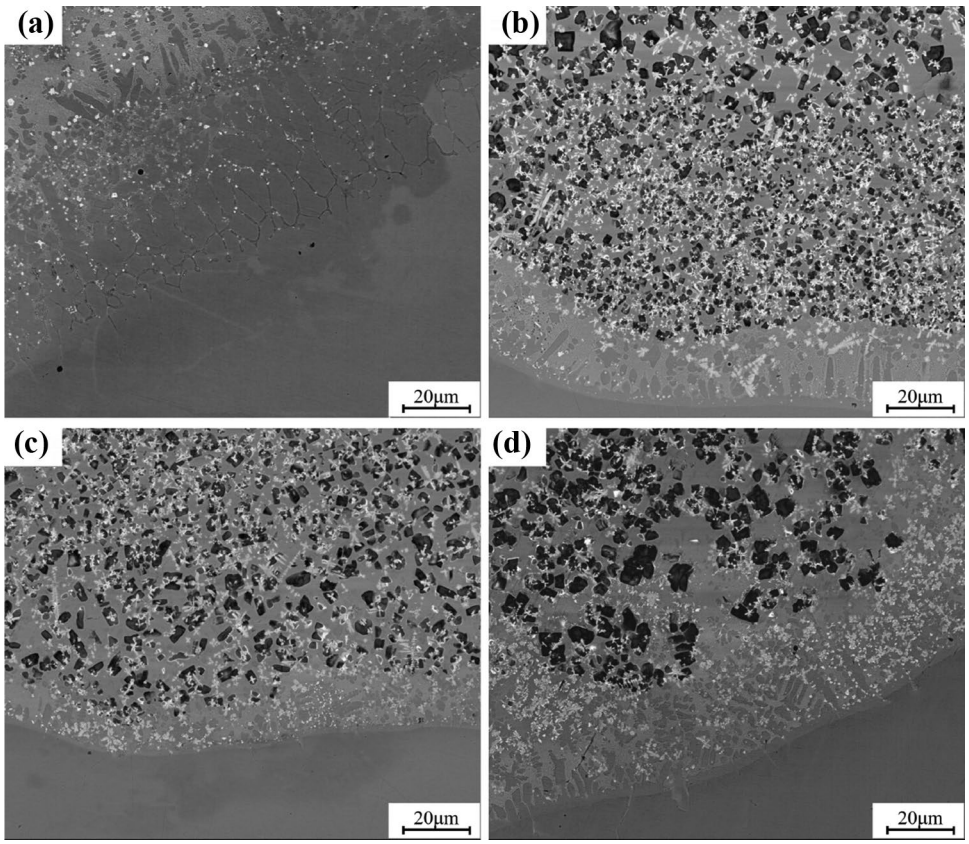

Fig. 10 Bonding zone BSE images of coatings: **a** C1, **b** C2, **c** C3, and **d** C4

the white phase; it can be summarized that the white phase in the coating with Nb addition was not only composed of TiC and W_2CoB_2 but also composed of NbC, (Nb,Ti,W)C, and slight Nb_2C.

Figure 10 shows the bonding zone BSE images of coatings. It was clearly to be found that the bottom region of all coatings had a columnar dendritic crystal structure, which was the typical coating microstructure in the laser cladding [45]. The molten pool convection has a significant effect on the microstructure of laser cladding layers. The columnar dendritic crystal structure can be formed due to the high energy in the molten pool and *G* (temperature gradient) and *R* (solidification rate); it can be found that the columnar dendritic crystal structure grew along the direction of heat dissipation [46]. The heat released during the solidification of the liquid phase was mainly dissipated through the substrate in the bonding zone, which resulted in the structures in the interface growing slowly upward in the form of a columnar dendritic crystal structure. During the laser cladding process, the powder absorbed high energy and formed a molten pool rapidly on the substrate. According to the solidification theory, the bottom of the molten pool had higher energy. Meanwhile, a larger *G* and a smaller *R* will lead to a large G/R ($\rightarrow \infty$), which resulted in the growth rate being larger than the nucleation rate to form a columnar dendritic crystal structure [47–49]. It was interesting to find that the bottom of C1 coating had the largest columnar dendritic crystal structure than others, which resulted from the high dilution rate.

To careful analyze the Nb distribution and phase component, a highly magnified SEM image corresponding to EPMA elemental maps is shown in Fig. 11. By comparing the positions of the different color-reinforced phase zones in the EPMA image in Fig. 11a, f, it can be observed that Nb was uniformly distributed in the white phase region, but it was almost nonexistent in the black phase or gray phase region. Results showed that the Nb element segregated near TiC particles. Also, the white phase had rich Ti and W; part of the internal Ti atoms and W atoms of the grains were replaced by Nb atoms to form carbide solid

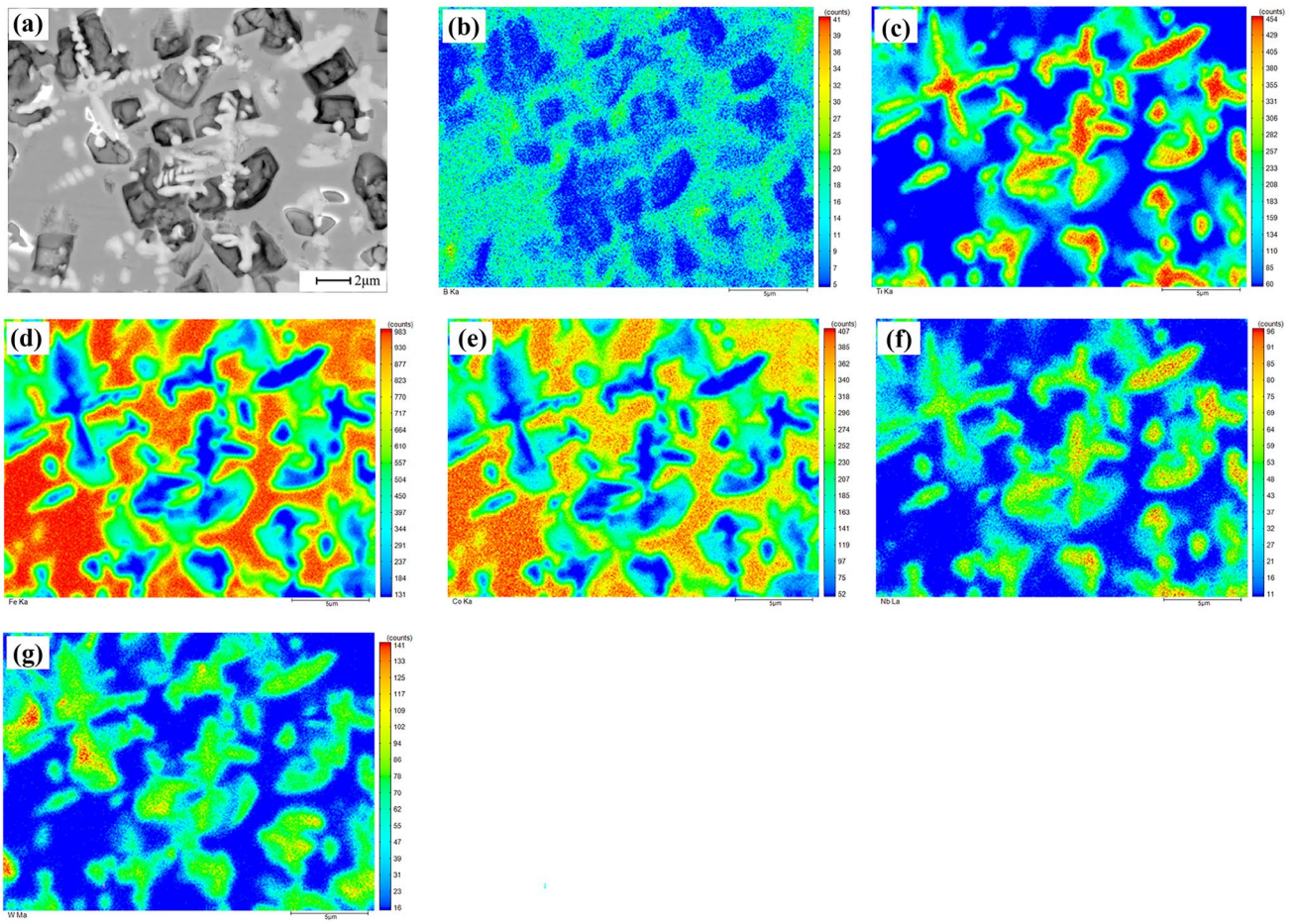

Fig. 11 **a** Highly magnified SEM image of the C3 coating; corresponding EPMA elemental maps showing the distribution of **b** B, **c** Ti, **c** Fe, **e** Co, **f** Nb, and **g** W

solutions [(Nb,Ti,W)C]. Besides, the B element mostly existed in the white phase although it had low content compared with other elements. The black phase and gray phase had high content of Fe element and Co element.

Combining the results of XRD, SEM, EDS, and EPMA, it can be concluded that the white phase was composed of TiC, W_2CoB_2, NbC, (Nb,Ti,W)C, and little Nb_2C. The gray phase was composed of $Fe_{11}Co_5$, Fe, and Co_2B, while the black phase was composed of $Fe_{11}Co_5$, Fe, and slight TiB_2 and WCoB.

3.3 Microhardness and fracture toughness

The microhardness of the coating was determined by the microstructure and reinforced phase content. The microhardness distribution in the thickness directions of coatings with different Nb additions is shown in Fig. 12. It can be found that the microhardness decreased from the top surface of the coating to the substrate, while some points showing the sudden increase of microhardness in the coating were probably due to the hard phase as tested by the probe. The microhardness of the coating with Nb addition was higher than that of without Nb addition, which proved that the Nb addition can improve the microhardness of the coating. According to the analysis results of XRD, EDS, SEM, and EPMA, the fine in-situ synthesized NbC, (Nb,Ti,W)C, and Nb_2C can increase the microhardness. Besides, the C3 coating had the highest microhardness due to its fine grain size. The microhardness of HAZ was higher than that of the substrate owing to the effect of dilution rate during the laser cladding.

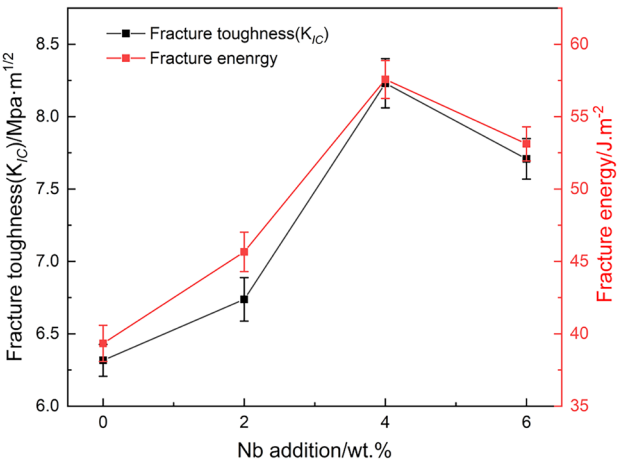

Fig. 13 The fracture toughness and fracture energy of coatings with different Nb additions

The fracture toughness (K_{IC}) refers to the ability to resist crack propagation. In order to evaluate the effect of Nb addition on the K_{IC} of the coating, the calculated K_{IC} and fracture energy of coatings are plotted in Fig. 13. It was clearly found that the K_{IC} increased firstly and then decreased sharply with the increase of Nb addition. When the Nb addition was 4 wt%, the coating had the highest K_{IC} (8.23 MPa m$^{1/2}$),

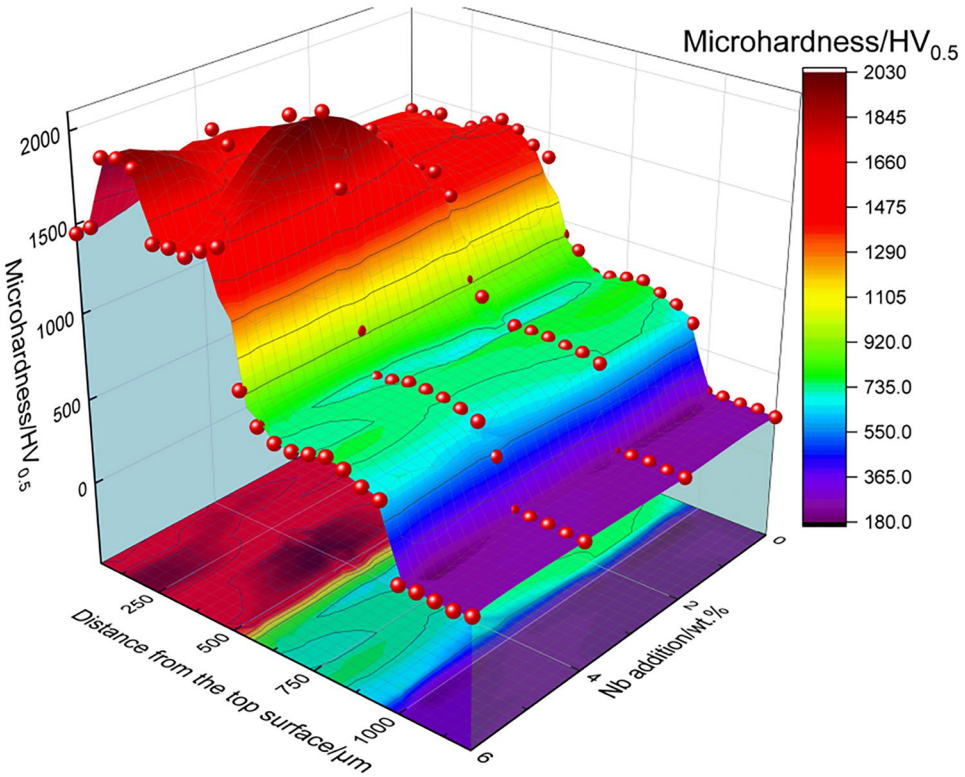

Fig. 12 Microhardness distribution in the thickness directions of coatings with different Nb additions

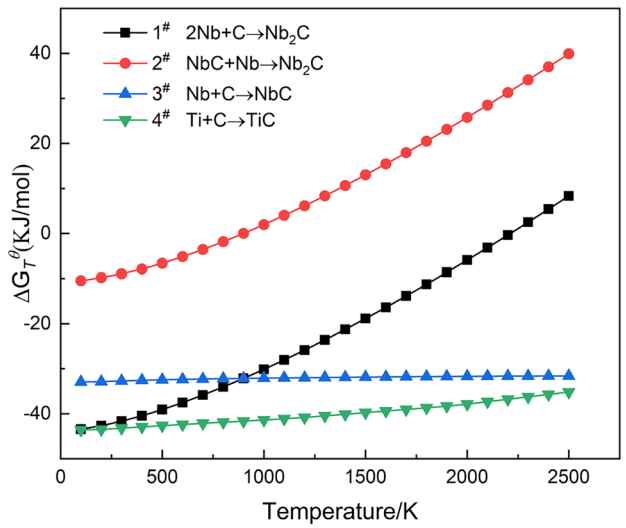

Fig. 14 The Gibbs free energy formation of NbC, Nb_2C, and TiC versus temperature for potential reactions

which was almost 30% higher than that of C1 coating. The reason for the increase or decrease of K_{IC} is discussed in Sect. 4.5. Among all coatings, C3 coating had the highest fracture energy (~57.57 J/m^2), which determined that it had the highest K_{IC}.

4 Discussion

4.1 Formation mechanism of reinforced phases

To better understand the mechanism of the in-situ reaction with NbC, Nb_2C, and TiC, the Gibbs free energy (ΔG_T^{θ}) formation of NbC, Nb_2C, and TiC versus temperature for potential reactions is shown in Fig. 14 [50–52]. According to the laws of thermodynamics, the direction and order of the chemical reaction can be judged by ΔG_T^{θ}. It can be seen that when the temperature (T) > 0, $\Delta G_{TiC}^{\theta}(4^{\#})$ was lower than $\Delta G_{NbC}^{\theta}(3^{\#})$, which indicated that TiC formed firstly than NbC during the laser cladding process. Besides, ΔG_{TiC}^{θ} and ΔG_{NbC}^{θ} were < 0, which indicated that TiC and NbC can be in-situ synthesized by the reaction of $4^{\#}$ and $3^{\#}$ [53, 54]. Hence, the C atom in the coating easily combined with Ti and Nb to form TiC and NbC. However, the formation of Nb_2C by the reaction of $1^{\#}$ and $2^{\#}$ was weaker than others, which indicated that the formation of Nb_2C was hard due to the limit of TiC and NbC, and this was consistent with the XRD results. Regardless of reaction $1^{\#}$ being more prone to occur than reaction $2^{\#}$, the increasing temperature suppressed the Nb_2C in-situ formation.

4.2 Elastic constants

Owing to the elastic constant difference of different strengthening phases from the existing research results, it is essential to evaluate the strengthened phases in the coating. Table 5 lists the calculated bulk modulus B (GPa), shear modulus G (GPa), Young's modulus E (GPa), Poisson's ratio ν, and hardness (GPa) of different strengthened phases. In addition, the hardness of strengthened phases can be calculated by the bulk modulus and shear modulus with a semi-empirical hard model as Eq. (6) [38, 55].

$$H_v = 0.92K^{1.137}G^{0.708} \quad (6)$$

where the Pugh's modulus ratio of K was introduced as G/B. The K value is often used to reflect the toughness of materials. Generally, the K value of brittle materials is less than 1.75 and more than 1.75 for metal materials [56]. The K value of Nb_2C is 1.91, which indicated that the tenacity of Nb_2C is excellent, and other strengthened phases are brittle materials. The ν of Nb_2C is 0.278, which reflected the strong metallicity [56].

4.3 Effect of grain size on the microhardness

It can be seen from Fig. 15a that the average grain size in the bottom region was relatively fine compared to the other regions, owing to the large G and smaller R being able to promote the formation of fine grain size. The solidification rate increased and the temperature rate decreased as the distance from the bottom to the top of the coating, which resulted in smaller G/R (→ 0). Hence, a coarse

Table 5 The calculated bulk modulus B (GPa), shear modulus G (GPa), Young's modulus E (GPa), Poisson's ratio ν, and hardness (GPa) of strengthened phases

Phase	B	G	B/G	E	ν	H_V
WCoB	345.19	201.51	1.71	506.06	0.256	21.353
W_2CoB_2	345.42	216.78	1.59	537.87	0.240	24.415
NbC	307.85	202.43	1.52	498.10	0.230	24.525
Nb_2C	232.60	121.49	1.91	310.44	0.278	13.151
TiC	253.28	166.65	1.52	410.02	0.230	21.285

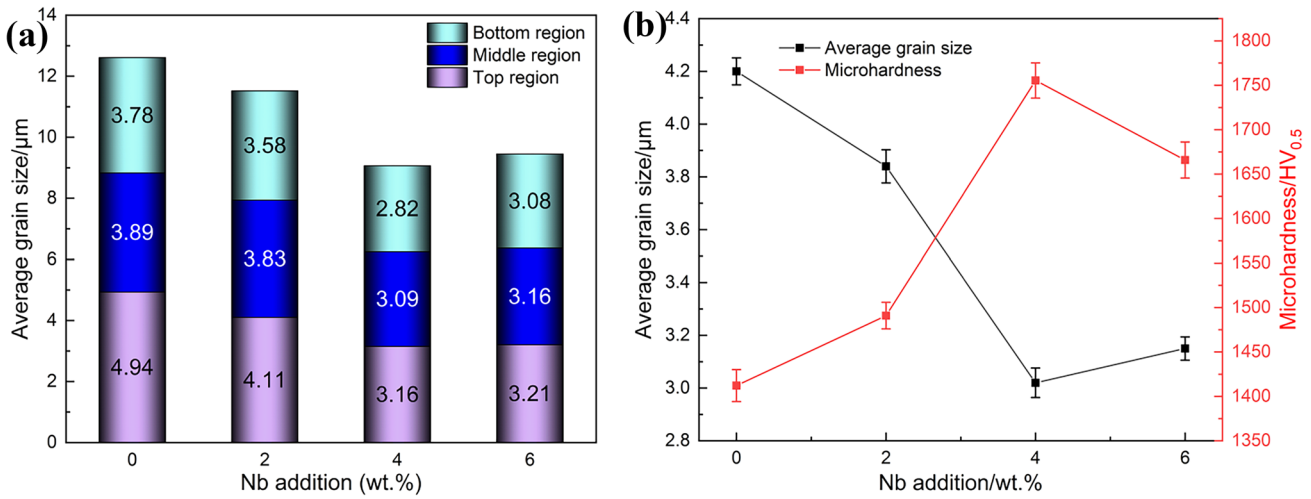

Fig. 15 The relationship of grain size and microhardness: **a** the average grain size of different regions of coatings; **b** the average grain size and microhardness of coatings

grain (dendritic crystal structure) was formed due to the growth rate being larger than the nucleation rate. The average grain size of all regions decreased firstly and then increased gradually with the increase of Nb addition, and the C3 coating had the best grain size. Combined with the results of microhardness (Fig. 12), the microhardness of the coating was larger than that of HAZ and substrate, and the microhardness decreased approximately from the top surface to the bottom of the coating. However, the sum content of the white phase and black phase in the top region, middle region, and bottom region of the C3 coating was 43.56%, 39.23%, and 32.38%, respectively. All coatings had a similar regular pattern of strengthening phases. According to the EDS and EPMA results, the black and white phases were mostly a hard phase, and the Nb element distributed in the white phase (TiC (21.285 GPa)) formed NbC (24.525 GPa), Nb_2C (13.151 GPa), and slight content of (Nb,Ti,W)C. Hence, the coating had higher content white phase and black phase, which can improve the coating microhardness.

The average grain size and microhardness of coatings are shown in Fig. 15b; the average microhardness of C1, C2, C3, and C4 was 1412.2 $HV_{0.5}$, 1490.92 $HV_{0.5}$, 1755.42 $HV_{0.5}$, and 1665.82 $HV_{0.5}$, respectively. According to the Hall–Petch formula, a fine grain size leads to a high hardness [57, 58], which agreed with the change of the average grain size in Fig. 15b. The effect of Nb on grain refinement increased the grain boundary ratio and the dislocation density in the coating. The dislocations began to move under the action of an external load, and when the dislocations moved to the vicinity of the grain boundary, the phenomenon of dislocation plugging will occur. A larger load was required when the dislocation needed to move further [59, 60]. Therefore, the addition of Nb increased the deformability of the coating and improved the microhardness of the coating. The microhardness of C3 coating was higher than that of C1 coating, which indicated that Nb addition appropriately can refine the internal grain size of the coating. When the Nb addition exceeded 4 wt%, the crystal grain began to agglomerate and caused the decrease of the microhardness in the C4 coating.

4.4 Fracture mechanism

In order to investigate the fracture mechanism changes in the coating with different Nb additions, BSE-SEM images of crack propagation morphology are demonstrated in Fig. 16. It can be found that the C1 coating had cracks without applied force in Fig. 8a, which will increase the ability of crack propagation. The regions with high stress will appear cracking under the action of the applied force [61]. All the fracture forms of all coatings were typical transgranular fracture, while the C1 coating had a wider and more straight fracture path than the others. The transgranular fracture was beneficial to improving the fracture toughness of the coating, especially in the applications of brittle materials [62]. It was interesting to find that the cracks almost propagated the black phase of the coating, due to its components (WCoB and TiB_2) and had no fine carbides.

According to the results of Fig. 13, the fracture toughness and fracture energy increased firstly and then decreased with the increase of Nb addition. Owing to the strong metallicity of Nb_2C ($B/G = 1.91$), this resulted in a fine fracture toughness. Hence, when in-situ synthesized Nb_2C appeared in the coating, the fracture toughness of the coating with Nb addition was improved. In addition, the fine carbides (NbC, TiC)

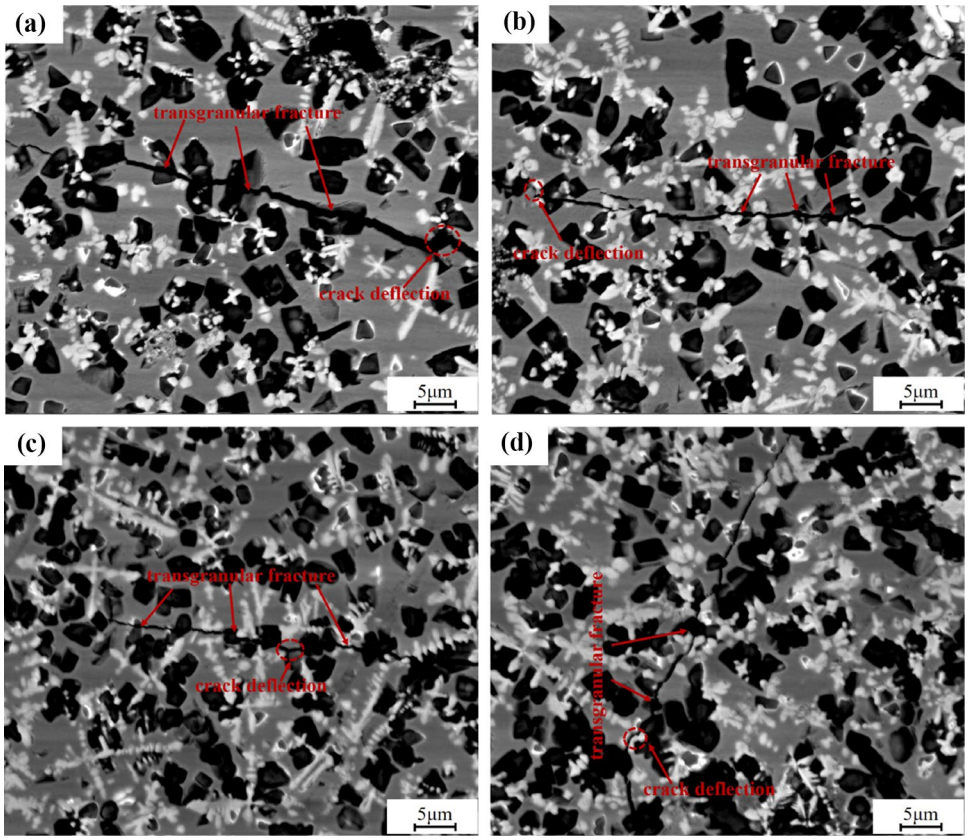

Fig. 16 BSE-SEM images of crack propagation morphology of coatings with different Nb additions: **a** 0 wt%, **b** 2 wt%, **c** 4 wt%, and **d** 6 wt%

and low porosity can also improve the fracture toughness of the coating. In general, the crack propagation will absorb more energy when the coating had more crack deflection, which led to the higher value of K_{IC} of the coating [63, 64]. When the cracks in the coating extended to the ceramic and metal interface, due to the different deformability, the cracks were locally passivated. Meanwhile, some of the cracks were forced to pass through the metal particles, which resulted in crack deflection to increase the fracture surface area and increased the crack propagation resistance [65]. Hence, it was beneficial to increase the fracture toughness of the coating. When the Nb addition was 6 wt%, the grain agglomeration had appeared in the coating, which will weaken the fracture toughness.

4.5 Microstructure evolution mechanism

In the laser cladding process of this study, the in-situ NbC, Nb_2C, TiC, WCoB, and W_2CoB_2 were dependent on the microstructure evolution. Thus, it is significant to study the microstructure evolution mechanism of the laser cladding. Sun et al. [50, 66] investigated the formation mechanism of NbC-reinforced Ni-based composites. The microstructure evolution steps can be expressed as shown in Fig. 17.

(a) The raw material and Nb composite powder were pre-placed on the surface of the AISI 1045 steel before laser cladding; the thickness of the pre-placed powder was controlled to about 1 mm.

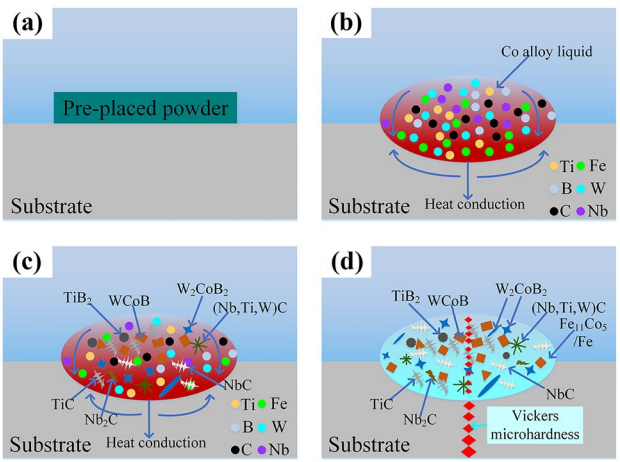

Fig. 17 The microstructure evolution mechanism of coating by laser cladding: **a** pre-placement of the cladding powders on the surface of AISI 1045 steel substrate; **b** the distribution and movement of atoms in the molten pool; **c** in-situ synthesized strengthened phases; **d** the coating at room temperature after laser cladding

(b) The Co powder has the lowest melting point among all powders of the study; thus, the Co powder melted firstly to form Co alloy liquid under the high laser energy in the initial stage of laser cladding. In addition, the excessive energy will promote the melting of other powders in the molten pool. Hence, the powder transformed to alloying element atoms by the Marangoni convection effect of continuous high temperature during the laser cladding process.

(c) As the continuation of laser cladding process, the elemental atoms moved quickly and combined with each other and began to form reinforced phases gradually, which not only formed WCoB and W_2CoB_2 phases but also formed carbide-reinforced phases during laser cladding. According to the Gibbs free energy formation of NbC, Nb_2C, and TiC in Fig. 14, the TiC phase was firstly in-situ synthesized due to its low ΔG_T^{θ}, which was generated by the reaction of C (provided from WC) and Ti (provided from TiB_2); the remaining C atoms reacted with Nb atoms to form NbC, Nb_2C, and (Nb,Ti,W)C. However, owing to the rapid heating rate and cooling rate, part of Nb powder cannot be melted due to its high melting point. The unmelted Nb will act as the substrate of new in-situ synthesized NbC nucleation, and the newly formed NbC particles grew with heterogeneous nucleation. TiB_2 cannot fully react with other atoms to form new phases; thus, part of the unmelted TiB_2 powder decomposed and re-nucleated under the action of the high energy of laser cladding, and finally remained in the cladding layer in the form of TiB_2.

(d) The Fe atoms diffused into the coating and re-nucleated with Co atoms to form $Fe_{11}Co_5$, which resulted in the decrease of temperature in the coating. All the in-situ synthesized processes were finished when the temperature decreased to room temperature, and a reliable metallurgical bonding with the substrate was formed. Besides, the Vickers microhardness variation is shown in Fig. 17d in the form of indentation sizes. In the WCoB-TiC coating, it can be found that the hard phases improved the microhardness, indicated by the size of indentations. The indentation sizes became smaller in the hard phase zone than that of other zones in the coating. In the substrate, the indentation sizes became larger while the indentations were performed deeper in the substrate away from the bottom region of the coating, indicating the decrease of microhardness, which was consistent with the results of Sect. 3.3.

5 Conclusions

In-situ NbC particle–reinforced WCoB-TiC composite coating can be produced by laser cladding. A reliable metallurgical bonding can be obtained between the coating and the AISI 1045 steel substrate. The geometric characteristics, microstructure, microhardness, fracture toughness, and microstructure evolution mechanism of coatings were discussed in this study. The following conclusions can be drawn:

The morphologies and XRD were utilized to determine the content of alloy elements in the composite powders. With the increase of Nb addition, the dilution rate and porosity decreased gradually. The coating was mainly composed of WCoB, W_2CoB_2, TiC, TiB_2, Co_2B, Fe, and $Fe_{11}Co_5$. With the Nb added in the powder, the peaks of NbC, Nb_2C, and (Nb,Ti,W)C appeared in the coating.

The in-situ synthesized NbC, Nb_2C, and (Nb,Ti,W)C were distributed uniformly in the TiC columnar dendritic crystal structure. The content of reinforced phases decreased from the bottom to the top of the coating. The microhardness and fracture toughness increased firstly and then decreased gradually; when the Nb addition was 4 wt%, the coating had the highest microhardness and fracture toughness (1755.42 $HV_{0.5}$, 8.23 MPa $m^{1/2}$, respectively). The microhardness and fracture toughness was 24% and 30% higher than that of the coating without Nb addition. Plus, all the coating fracture mechanism was transgranular fracture.

According to the formation mechanism of reinforced phases, TiC formed firstly before NbC and Nb_2C. NbC had the highest hardness (24.525 GPa) of all in-situ synthesized reinforced phases, while Nb_2C had the best metallicity due to its high B/G (1.91) by the results of first principles calculation.

Microstructure evolution revealed that the morphology of the coating was determined by the atom diffusion, temperature gradient, and formation mechanism of reinforced phases. TiC was in-situ synthesized firstly in the molten pool, and then NbC formed gradually, while other C atoms in the coating formed Nb_2C or (Nb,Ti,W)C solid solution. The unmelted Nb acted as the substrate of new in-situ synthesized NbC nucleation.

Author contribution Hao Zhang: Methodology, investigation, formal analysis, writing – original draft. Yingjun Pan: Formal analysis, writing – original draft, writing – review and editing, supervision. Yang Zhang: Formal analysis, writing – original draft, writing – review and editing. Guofu Lian: Formal analysis, writing – original draft, writing – review and editing, funding acquisition. Qiang Cao: Investigation, formal analysis. Xingyu Zhu: Formal analysis.

Funding This study was supported by the National Natural Science Foundation of China (No. 51575110).

Availability of data and material All related data and materials are available in the manuscript text.

Declarations

Ethics approval Not applicable.

Consent to participate Not applicable.

Consent for publication Not applicable.

Conflict of interest The authors declare no competing interests.

References

1. Wu H, Zheng Y, Zhang J, Zhang G, Ke Z, Xu X, Lu X (2020) Influence of Cr and W addition on microstructure and mechanical properties of multi-step sintered Mo_2FeB_2-based cermets. Ceram Int 46:10963–10970
2. Jin J, Sun J, Wang G (2019) Effect of Mo content on microstructure and wear resistance of Mo-Fe-B claddings. Int J Refract Met Hard Mater 81:233–241
3. Zheng X-Q, Liu Y (2019) Slurry erosion–corrosion wear behavior in SiC-containing NaOH solutions of Mo_2NiB_2 cermets prepared by reactive sintering. Int J Refract Met Hard Mater 78:193–200
4. Yuan B, Zhang G-J, Kan Y-M, Wang P-L (2010) Reactive synthesis and mechanical properties of Mo_2NiB_2 based hard alloy. Int J Refract Met Hard Mater 28:291–296
5. Zhang J, Zheng Y, Zhou W, Zhang G, Ke Z, Dong Z, Feng P (2018) Effects of Cr content on the microstructure and mechanical properties of Mo_2FeB_2-based cermets prepared via vacuum sintering. Vacuum 155:509–513
6. Takagi K-I, Koike W, Momozawa A, Fujima T (2012) Effects of Cr on the properties of Mo_2NiB_2 ternary boride. Solid State Sci 14:1643–1647
7. Zhang L, Huang Z, Liu Y, Shen Y, Li K, Cao Z, Ren Z, Jian Y (2019) Effect of Ni content on the microstructure, mechanical properties and erosive wear of Mo_2NiB_2–Ni cermets. Ceram Int 45:19695–19703
8. Zhang L, Huang ZF, Shen YP, Li KM, Cao Z, Jian YX, Ren ZJ (2019) High-temperature compressive properties and tribological behaviour of Mo_2NiB_2–Ni cermets. Ceram Int 45:18413–18421
9. Wei X, Chen Z, Zhong J, Xiang Y (2016) Feasibility of preparing Mo_2FeB_2-based cermet coating by electrospark deposition on high speed steel. Surf Coat Technol 296:58–64
10. Xuming P, Yong Z, Shaogang W, Qiuhong W (2009) Effect of Mn on valence-electron structure and properties of hard phase in Mo_2FeB_2-based cermets. Int J Refract Met Hard Mater 27:777–780
11. Yu H, Zheng Y, Liu W, Zheng J, Xiong W (2010) Effect of Mn content on the microstructure and mechanical properties of Mo_2FeB_2 based cermets. Int J Refract Met Hard Mater 28:286–290
12. Yan X, Wang H, Liu X, Hou C, Qiu Q, Song X (2019) High-temperature oxidation and wear resistance of WC-Co based coatings with WB addition. J Eur Ceram Soc 39:3023–3034
13. Johnston JM, Catledge SA (2016) Metal-boride phase formation on tungsten carbide (WC-Co) during microwave plasma chemical vapor deposition. Appl Surf Sci 364:315–321
14. Zhang T, Yin H-Q, Zhang C, Qu X-H, Zheng Q-J (2018) Effect of Mn doping on mechanical properties and electronic structure of WCoB ternary boride by first-principles calculations. Chin Phys B 27:107101
15. Sáez A, Arenas F, Vidal E (2003) Microstructure development of WCoB–TiC based hard materials. Int J Refract Met Hard Mater 21:13–18
16. Liu X, Feng H, Hou C, Wang H, Chen J, Lu H, Song X (2020) Performance enhancement of ultra-coarse cemented carbide by boride additives. J Alloys Compd 835:155250
17. Yuan C, Yin H, Yang G, Yang X, Xu B, Deng Z, Liu Y, Li W, Zhang C, Zhang R, Qu X (2021) Tracking the evolution of microstructure and phases of WCoB-Co cermets during sintering. Int. J. Refract. Met. Hard Mater. 98:105550
18. Zhang T, Yin H, Zhang C, Zhang R, Yang Z, Elder S, Jiang X, Deng Z, Yang G, Zheng Q, Qu X (2019) Synthesis and microstructure evolution of WCoB based cermets during spark plasma sintering. Ceram Int 45:17536–17544
19. Jian Y, Huang Z, Liu X, Xing J (2019) Comparative investigation on the stability, electronic structures and mechanical properties of Mo_2FeB_2 and Mo_2NiB_2 ternary borides by first-principles calculations. Results Phys. 15:102698
20. Yu H, Liu W, Zheng Y (2011) Effect of carbon content on the microstructure and mechanical properties of Mo_2FeB_2 based cermets. Int J Refract Met Hard Mater 29:724–728
21. Zhang T, Yin H, Zhang C, Qu X (2020) Microstructure and mechanical properties of Cr doped WCoB based cermets by spark plasma sintering and first principle calculation. Prog Nat Sci Mater Int 30:417–423
22. Wang H, Yan X, Liu X, Lu H, Hou C, Song X, Nie Z (2018) Microstructure, mechanical and tribological properties of WC-WCoB coating. J Eur Ceram Soc 38:4874–4881
23. Li K, Li T, Ma M, Wang D, Deng W, Lu H (2021) Laser cladding state recognition and crack defect diagnosis by acoustic emission signal and neural network. Opt Laser Technol 142:107161
24. Lv H, Li X, Li Z, Wang W, Yang K, Li F, Xie H (2021) Investigation on the columnar-to-equiaxed transition during laser cladding of IN718 alloy. J Manuf Process 67:63–76
25. Qi K, Yang Y, Liang W, Jin K, Xiong L (2021) Effect of magnetic field on the microstructure and wear properties of TiB_2/metal composite layers synthesized in situ by laser cladding on Ti–6Al–4V alloy. Ceram Int (In Press)
26. Liu X, Bi J, Meng Z, Li R, Li Y, Zhang T (2021) Tribological behaviors of high-hardness Co-based amorphous coatings fabricated by laser cladding. Tribol Int 162:107142
27. Shen C, Li C, Guo Y, Liu C, Zhang X, Feng X (2021) Modeling of temperature distribution and clad geometry of the molten pool during laser cladding of TiAlSi alloys. Opt Laser Technol 142:107277
28. Ren W, Zhuang B, Lei W, Cao Q (2021) Microstructure and performance evolution of Ti-6Al4 V alloy coating by laser cladding and laser shocking composite remanufacture. Opt Laser Technol 143:107342
29. Chai Q, Wang Z, Fang C, Xing Y, Qiu X, Zhou Z (2021) Numerical and experimental study on the profile of metal alloys formed on the inclined substrate by laser cladding. Surf Coat Technol 422:127494
30. Yan G, Zheng M, Ye Z, Gu J, Li C, Wu C, Wang B (2021) In-situ Ti(C, N) reinforced AlCoCrFeNiSi-based high entropy alloy coating with functional gradient double-layer structure fabricated by laser cladding. J Alloys Compd 886:161252
31. Hu D, Liu Y, Chen H, Wang M, Liu J (2021) Microstructure and properties of in-situ synthesized Ni3Ta-TaC reinforced Ni-based coatings by laser cladding. Surf Coat Technol 405:126599
32. Liu H, Liu J, Chen P, Yang H (2019) Microstructure and high temperature wear behaviour of in-situ TiC reinforced AlCoCrFeNi-based high-entropy alloy composite coatings fabricated by laser cladding. Opt Laser Technol 118:140–150
33. Xiao DH, He YH, Song M, Lin N, Zhang RF (2010) Y_2O_3- and NbC-doped ultrafine WC–10Co alloys by low pressure sintering. Int J Refract Met Hard Mater 28:407–411
34. Genga RM, Cornish LA, Woydt M, Janse van Vuuren A, Polese C (2018) Microstructure, mechanical and machining properties of LPS and SPS NbC cemented carbides for face-milling of grey cast iron. Int J Refract Met Hard Mater 73:111–120

35. Wu Y, He W, Guo H (2020) Improved fracture toughness and multiple toughening mechanisms of $NdPO_4$/$NdYbZr_2O_7$ composites. Ceram Int 46:16612–16619
36. Wu Y, Zheng L, He W, He J, Guo H (2019) Effects of Yb^{3+} doping on phase structure, thermal conductivity and fracture toughness of $(Nd_{1-x}Yb_x)_2Zr_2O_7$. Ceram Int 45:3133–3139
37. Li C, Ma Y, He J, Guo H (2019) Self-toughening behavior of nano yttria partially stabilized hafnia ceramics. Ceram Int 45:21467–21474
38. Wang G, Jiang Y, Li Z, Chong X, Feng J (2021) Balance between strength and ductility of dilute Fe_2B by high-throughput first-principles calculations. Ceram Int 47:4758–4768
39. Zhang X, Wang D, Zhou Y, Chong X, Li X, Zhang H, Nagaumi H (2021) Exploring crystal structures, stability and mechanical properties of Fe, Mn-containing intermetallics in Al-Si Alloy by experiments and first-principles calculations. J Alloys Compd 876:160022
40. Lu K, Shen C, He Y, Huang S, Ba Y (2021) Effect of solute elements (Cr, Mo, Fe, Co) on the adhesion properties of WC/Ni-based binder interface: a first-principles study. Int J Refract Met Hard Mater 98:105563
41. Zhang J, Su C, Chen X, Liu H, Zhang L (2021) First-principles study on pitting corrosion of Al deoxidation stainless steel with rare earth element (La) treatment. Mater Today Commun 27:102204
42. Hu Y, Wang L, Yao J, Xia H, Li J, Liu R (2020) Effects of electromagnetic compound field on the escape behavior of pores in molten pool during laser cladding. Surf Coat Technol 383:125198
43. Chen Z, Yan H, Zhang P, Yu Z, Lu Q, Guo J (2019) Microstructural evolution and wear behaviors of laser-clad Stellite 6/NbC/h-BN self-lubricating coatings. Surf Coat Technol 372:218–228
44. Zhou W, Xiong J, Wan W, Guo Z, Lin Z, Huang S, Tang L, Zhong H (2015) The effect of NbC on mechanical properties and fracture behavior of WC–10Co cemented carbides. Int J Refract Met Hard Mater 50:72–78
45. Li Q, Lei Y, Fu H (2014) Laser cladding in-situ NbC particle reinforced Fe-based composite coatings with rare earth oxide addition. Surf Coat Technol 239:102–107
46. Wang Q, Yang J, Niu W, Li Y, Mao X, Wang Y, Zhang K (2021) Effect of La_2O_3 on microstructure and properties of Fe-based alloy coatings by laser cladding. Optik 245:167653
47. Jelvani S, Shoja Razavi R, Barekat M, Dehnavi MR, Erfanmanesh M (2019) Evaluation of solidification and microstructure in laser cladding Inconel 718 superalloy. Opt Laser Technol 120:105761
48. Cao Y, Farouk N, Taheri M, Yumashev AV, Bozorg SFK, Ojo OO (2021) Evolution of solidification and microstructure in laser-clad IN625 superalloy powder on GTD-111 superalloy. Surf Coat Technol 412:127010
49. Thawari N, Gullipalli C, Katiyar JK, Gupta TVK (2021) Effect of multi-layer laser cladding of Stellite 6 and Inconel 718 materials on clad geometry, microstructure evolution and mechanical properties. Mater Today Commun 28:102604
50. Sun S, Fu H, Ping X, Guo X, Lin J, Lei Y, Wu W, Zhou J (2019) Formation mechanism and mechanical properties of titanium-doped NbC reinforced Ni-based composite coatings. Appl Surf Sci 476:914–927
51. Zhao N, Xu Y, Fu Y (2017) Mechanical properties of one-step in situ synthesized NbC-Fe composite coating. Surf Coat Technol 309:1105–1110
52. Cai X, Xu Y (2017) Microstructure, friction and wear of NbC coatings on a Fe substrate fabricated via an in situ reaction. Surf Coat Technol 322:202–210
53. Wang X-L, Shao Y-X, Guo M-Y, Yang Y, Ma Y-D, Cui Y-H, Sun W-W, Dong Y-C, Yan D-R (2021) Comparison of plasma sprayed NbB_2-NbC coatings obtained by ex-situ and in-situ approaches. J Eur Ceram Soc 41:5088–5099
54. Yu HL, Zhang W, Wang HM, Ji XC, Song ZY, Li XY, Xu BS (2017) In-situ synthesis of TiC/Ti composite coating by high frequency induction cladding. J Alloys Compd 701:244–255
55. Zhao C, Zhou Y, Xing X, Liu S, Ren X, Yang Q (2018) Investigation on the relationship between NbC and wear-resistance of Fe matrix composite coatings with different C contents. Appl Surf Sci 439:468–474
56. Liu H, Yuan X, Rao L, Liu S, Shi Z, Zhou Y, Yang Q (2019) Refinement mechanism of NbC by CeO_2 in hypereutectic Fe-Cr-C hardfacing coating. J Alloys Compd 770:1016–1028
57. Gao Y, Yan M-Y, Luo B-H, Ouyang S, Chen W, Bai Z-H, Jing H-B, Zhang W-W (2017) Effects of NbC additions on the microstructure and properties of non-uniform structure WC-Co cemented carbides. Mater Sci Eng A 687:259–268
58. Huang JH, Huang SG, Zhou P, Lauwers B, Qian J, Vleugels J (2021) Microstructure and mechanical properties of WC or Mo_2C modified NbC-Ni cermets. Int J Refract Met Hard Mater 95:105440
59. Zhao LZ, Zhao MJ, Song LJ, Mazumder J (2014) Ultra-fine Al–Si hypereutectic alloy fabricated by direct metal deposition. Mater Des 56:542–548
60. Yi P, Zhan X, He Q, Liu Y, Xu P, Xiao P, Jia D (2019) Influence of laser parameters on graphite morphology in the bonding zone and process optimization in gray cast iron laser cladding. Opt Laser Technol 109:480–487
61. Cai X, Zhong L, Xu Y, Li X, Liu M (2019) Microstructure and fracture toughness of a WC-Fe cemented carbide layer produced by a diffusion-controlled reaction. Surf Coat Technol 357:784–793
62. Weng Z, Gu K, Wang K, Liu X, Cai H, Wang J (2019) Effect of deep cryogenic treatment on the fracture toughness and wear resistance of WC-Co cemented carbides. Int J Refract Met Hard Mater 85:105059
63. Qian C, Li K, Cheng H, Zhang W, Jiang X, Liu Y (2021) Fracture behavior of cemented carbides with CoNiFe medium entropy alloy binder. Int J Refract Met Hard Mater 98:105547
64. Lu Z, Du J, Sun Y, Su G, Zhang C, Kong X (2021) Effect of ultrafine WC contents on the microstructures, mechanical properties and wear resistances of regenerated coarse grained WC-10Co cemented carbides. Int J Refract Met Hard Mater 97:105516
65. Li D, Liu Y, Ye J, Chen X, Wang L (2021) The enhancement of the microstructure and mechanical performances of ultrafine WC-Co cemented carbides by optimizing Cr2(C, N) addition and WC particle sizes. Int J Refract Met Hard Mater 97:105518
66. Sun S, Fu H, Ping X, Lin J, Lei Y, Wu W, Zhou J (2018) Reinforcing behavior and microstructure evolution of NbC in laser cladded Ni45 coating. Appl Surf Sci 455:160–170